Journal of Structural Geology 33 (2011) 1178–1192

Contents lists available at ScienceDirect

Journal of Structural Geology

journal homepage: www.elsevier.com/locate/jsg

Effect of finite strain on clast-based vorticity gauges

Donald W. Stahr III *, Richard D. Law

Department of Geosciences, Virginia Tech, Blacksburg, VA 24061, USA

ARTICLE INFO

Article history:
Received 28 September 2010
Received in revised form
29 March 2011
Accepted 8 May 2011
Available online 13 May 2011

Keywords:
Ductile flow
Mylonite
Numerical model
Rigid clasts
Strain
Vorticity analysis

ABSTRACT

Clast-based vorticity gauges utilize orientations of grains assumed to have behaved as isolated rigid particles suspended in a flowing viscous matrix. A fundamental assumption behind use of the method is that sufficient strain has accumulated for high aspect ratio grains to rotate into positions approaching their stable sink orientation, and that clasts below a critical aspect ratio may be observed in any orientation relative to the flow plane. We constructed a numerical model to explore the effect of variable finite strain on development of the orientation distribution of a large population of rigid clasts embedded in a viscous medium for end-member pure and simple shear and for several distinct general shear flows. Our model predicts the technique will tend to produce vorticity overestimates for lower vorticity flows for a wide range of finite strain. The model also indicates that clast populations in moderate to high vortical flows tend to develop shape preferred orientations that closely resemble those expected for flows of lower vorticity. We conclude that clast-based methods are not effective for extracting detailed kinematic information from a mylonite deformed in a flow with arbitrary boundary conditions. In fact, it appears that most general shear flows continued long enough to develop moderate–high finite strains will tend to produce a clast orientation distribution that will yield a visual estimate of the critical aspect ratio that suggests approximately equal contributions of pure and simple shear components.

1. Introduction

Since the introduction of kinematic vorticity into the geological literature (McKenzie, 1979; Means et al., 1980), and the development of methods for extracting these data from naturally deformed rocks (e.g., Passchier, 1986, 1987; Vissers, 1989; Wallis, 1992; Wallis et al., 1993; Simpson and De Paor, 1993), structural studies of orogenic belts have increasingly focused on determining the boundary conditions of flow during ductile deformation in high-strain zones. Results of these investigations have repeatedly shown crustal-scale shear zones from a wide array of tectonic settings involved a departure from ideal simple shear (e.g., Passchier, 1987; Vissers, 1989; Wallis et al., 1993; Xypolias and Doutsos, 2000; Law et al., 2004; Jessup et al., 2006, 2007; Bailey et al., 2007; Johnson et al., 2009). The implications of these results are significant for several reasons. Consider a shallowly dipping mylonite zone, a common feature in orogenic hinterlands, deforming by simultaneous pure and simple shearing [here we follow previous authors (e.g., Ramberg, 1975) in using the *suffix-ing* to emphasize terms related to the deformation process]. The pure shearing component of an isochoric, plane strain, sub-simple shearing deformation causes thinning perpendicular to the zone boundaries. Strain compatibility arguments require that material must simultaneously stretch parallel to the shear zone boundary. Material in such a narrowing-lengthening shear zone (Simpson and De Paor, 1993; Tikoff and Fossen, 1999) is likely directed toward the synorogenic topographic surface, causing a material flux from lower to higher crustal levels (i.e., from orogenic core to foreland). Purely geometric arguments indicate the magnitude and rate of extrusion of material increase rapidly from the core to foreland of the orogen forcing an increase in strain rate at higher structural levels (Law, 2010). Such coupling of middle and shallow crustal levels may help drive deformation in the orogenic foreland. This simple example illustrates that reliable methods of determining kinematic parameters from high-strain zones are critically important for meaningful interpretation of structural evolution within such ductile deformation zones.

Several vorticity gauges, including: (1) deformed vein sets (Talbot, 1970; Hutton, 1970; Passchier, 1986); (2) clast-based gauges (Passchier, 1987; Simpson and De Paor, 1993; Wallis et al., 1993); (3) quartz petrofabric and strain ratio (R_{XZ}/β) (Wallis, 1992, 1995); (4) oblique dynamically recrystallized grain shape foliation (Wallis, 1995); R_{XZ}/δ method of (Xypolias (2009, 2010); (5) angle between macroscopic foliation and shear zone boundary (R_{XZ}/θ) (Tikoff and Fossen, 1995); and (6) flanking structures (Grasemann and Stüwe, 2001) have been applied to natural rocks. Clast-based vorticity

* Corresponding author. Tel.: +1 5402319740; fax: +1 5402313386.
E-mail address: dstahr@vt.edu (D.W. Stahr).

0191-8141/$ – see front matter © 2011 Elsevier Ltd. All rights reserved.
doi:10.1016/j.jsg.2011.05.002

gauges are the most commonly applied to natural samples due to: (1) their relative simplicity and rapid application; and (2) many of the assumptions required for the technique to be valid are apparently met (see Passchier, 1987). Early theoretical models published by Masuda et al. (1995) indicated that clast-based techniques may be useful to broadly discriminate between coaxial and non-coaxial flow. However, even with the increased use during the last 15 years (e.g., Passchier, 1987; Vissers, 1989; Wallis et al., 1993; Simpson and De Paor, 1997; Holcombe and Little, 2001; Xypolias and Koukouvelas, 2001; Bailey and Eyster, 2003; Law et al., 2004; Carosi et al., 2006; Jessup et al., 2006, 2007; Xypolias and Kokkalas, 2006; Bailey et al., 2007; Marques et al., 2007; Thigpen et al., 2010), no advance has been made on understanding the role finite strain plays on the evolution of clast orientation distributions for different flow types.

Finite strain magnitude is critically important in all vorticity estimation methods as it is either an explicit parameter (e.g., R_{XZ}/θ, R_{XZ}/β, and R_{XZ}/δ methods), or for the clast-based method in particular, it is tacitly assumed that sufficient strain has accumulated for high aspect ratio grains to have rotated into their stable positions. Because finite strain is a fundamental parameter for determining the porphyroclast orientation distribution produced during deformation, we view the lack of knowledge of strain state as a limit on the usefulness of vorticity estimates made solely from clast-based techniques, and argue that multiple techniques should be used to constrain deformation kinematics.

In this paper we first review the mathematical theory necessary to describe pure, simple, and sub-simple shearing flow and use this theoretical framework to model a large population of rigid elliptical objects in viscous flows of variable kinematic vorticity and at a wide range of finite strains. Our primary interest lies in discovering if there exists a single value of finite strain necessary to produce a well-organized orientation distribution for different flow types. To this end we applied the governing equations (and therefore assumptions and limitations) derived in the seminal paper by Ghosh and Ramberg (1976). Some surprising behavior is predicted at moderate to high kinematic vorticity and high finite strains. Implications of these results are discussed in a geological context.

2. Mathematical framework

2.1. Description of flow and progressive deformation

The velocity field about a point in a deforming continuum is described by the velocity gradient tensor, **L**,

$$\mathbf{v} = \mathbf{L}\mathbf{x} \tag{1}$$

where **v** is a velocity vector, or the time derivative of position vector **x** (i.e., $\mathbf{v} = d\mathbf{x}/dt$). The associated velocity gradient equations become (Means et al., 1980):

$$v_i = L_{ij}x_j \tag{2}$$

where v_i are the velocity components at position x_j at an instant in time, and

$$L_{ij} = \frac{\partial v_i}{\partial x_j} = \begin{bmatrix} L_{11} & L_{12} \\ L_{21} & L_{22} \end{bmatrix}$$

(see Malvern, 1969, p. 146) are the spatial velocity gradients for a two-dimensional flow (see Fig. 1). If the velocity gradient tensor components L_{ij} are constant the flow is homogeneous (Means et al., 1980). For isochoric plane strain monoclinic flow with simultaneous pure and simple shearing, **L** may be written as

$$\mathbf{L} = \begin{bmatrix} \dot{\varepsilon}_x & \dot{\gamma} \\ 0 & \dot{\varepsilon}_y \end{bmatrix} \tag{3}$$

where $\dot{\varepsilon}_x$ is the pure shearing strain rate and $\dot{\gamma}$ is the simple shearing strain rate, here taken perpendicular and parallel to the abscissa, respectively. Setting $\dot{\varepsilon}_y = -\dot{\varepsilon}_x$ forces the deforming material to be incompressible. The eigenvectors, ξ_i, of **L** give the orientations of the flow apophyses (Ramberg, 1975; Passchier, 1988).

The velocity gradient tensor, **L**, may be decomposed into the symmetric stretching tensor, $\dot{\mathbf{S}}$, and skew-symmetric vorticity tensor, **W** (Malvern, 1969, p. 147; Bobyarchick, 1986)

$$\mathbf{L} = \dot{\mathbf{S}} + \mathbf{W} \tag{4}$$

where

$$\dot{\mathbf{S}} = \begin{bmatrix} \dot{\varepsilon}_x & \frac{1}{2}\dot{\gamma} \\ \frac{1}{2}\dot{\gamma} & \dot{\varepsilon}_y \end{bmatrix} \tag{5}$$

and

$$\mathbf{W} = \begin{bmatrix} 0 & \frac{1}{2}\dot{\gamma} \\ -\frac{1}{2}\dot{\gamma} & 0 \end{bmatrix}. \tag{6}$$

The eigenvectors and eigenvalues of $\dot{\mathbf{S}}$ provide information on the orientation and magnitude of the instantaneous stretching axes (ISA_i) and instantaneous stretching rates ($\dot{s}_i$) of the flow, respectively. The vorticity tensor, **W**, has components of angular velocity and describes the rotation rate of elements in the deforming material.

The kinematic vorticity number, W_k, is a useful way of quantifying the instantaneous non-coaxiality of the flow at a point in space and an instant in time, and has a unique value for any distinct flow. By definition, W_k is an instantaneous quantity, but for the steady flows considered here the vorticity number remains constant during progressive deformation. The quantity s_r, defined as the ratio of pure to simple shearing strain rate, $s_r = \dot{\varepsilon}_x/\dot{\gamma}$ (Ghosh and Ramberg, 1976), is also a measure of the degree of non-coaxiality of the flow and may be expressed as a function of the kinematic vorticity number by the relation (Ghosh, 1987, Eq. (9))

$$s_r = \frac{1}{2}\sqrt{\frac{1}{W_k^2} - 1}. \tag{7}$$

Conversely, the kinematic vorticity may be calculated from knowledge of the instantaneous pure and simple shearing strain rates by the relation

$$W_k = \cos\left[\tan^{-1}\left(2\frac{\dot{\varepsilon}_x}{\dot{\gamma}}\right)\right] \tag{8}$$

or more simply

$$W_k = \cos(\alpha) \tag{9}$$

where α is the acute angle between the eigenvectors (ξ_i) of **L** (for derivation see Bobyarchick, 1986). By choosing appropriate values for s_r or W_k we can form a velocity gradient tensor, **L**, to produce the velocity field of a deformation of any vorticity number of interest.

From (8) it is clear that identical W_k values result from any combination of $\dot{\varepsilon}_x$ and $\dot{\gamma}$ that yield the same s_r value. Thus, any choice of $\dot{\varepsilon}_x$ and $\dot{\gamma}$ that yield the same ratio give rise to identical velocity fields; only the time required to accumulate a finite strain state will vary. Note from (7) that s_r increases without bound as

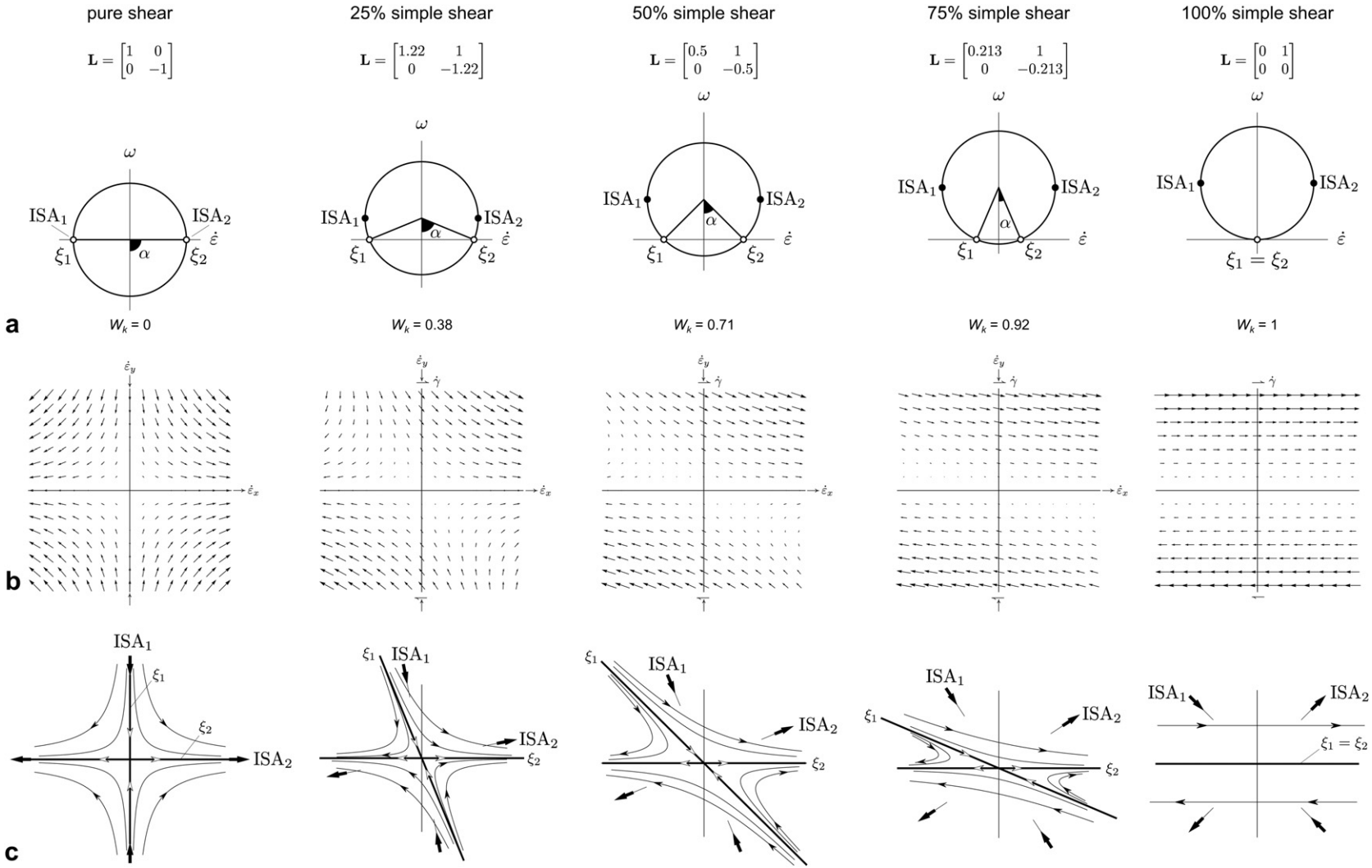

Fig. 1. Steady flows considered in this paper. (a) Mohr circle for given numerical **L** ($\dot{\varepsilon} - \omega$ space). Note that a constant value of unity is used as simple shearing strain rate ($\dot{\gamma}$) for simple shear and all general shear flows. Eigenvectors (ξ_i) of **L**, instantaneous stretching axes (ISA_i), and angle (α) between eigenvectors in real space indicated on Mohr construction. Percent simple shear and W_k number also indicated for each flow. (b) Velocity field in real space for associated **L**. Each arrow points in the direction of the velocity vector at the spatial point coincident with vector tail, and is scaled relative to velocity magnitude. (c) Representative particle paths for associated **L** and velocity field for each flow. Flow apophyses (labeled by coincident eigenvector) and ISA_i indicated. Arrows superimposed on curves indicate temporal evolution of particle positions. Thin curves represent hyperbolic particle paths of material points and thick curves represent straight-line particle paths directly toward or away from origin parallel to flow eigenvectors.

W_k approaches zero. Inspection of (8) and (9) reveals that W_k is a nonlinear function of s_r or α. W_k ranges from 0 ($\alpha = 90°$) for pure shearing to 1 ($\alpha = 0°$) for simple shearing (Fig. 2). Flows with $W_k > 1$, where the rotation component is greater than that for strict simple shear, are also possible but are not considered here.

The position gradient tensor, **D**, relates the position of a particle in the deformed state, **x**′, to its position in the undeformed state, **x**:

$$\mathbf{x}' = \mathbf{D}\mathbf{x}. \tag{10}$$

Provost et al. (2004) have shown that a relationship between **L** and **D** exists in the form

$$\mathbf{D} = \exp[\mathbf{L}\Delta t] \tag{11}$$

where $\Delta t = t - t_0$ is the time elapsed since the onset of deformation (or since a previously deformed state). It is therefore possible to use this relationship to determine the position of a particle at any time t for a given flow. If we let deformation begin at $t_0 = 0$ then

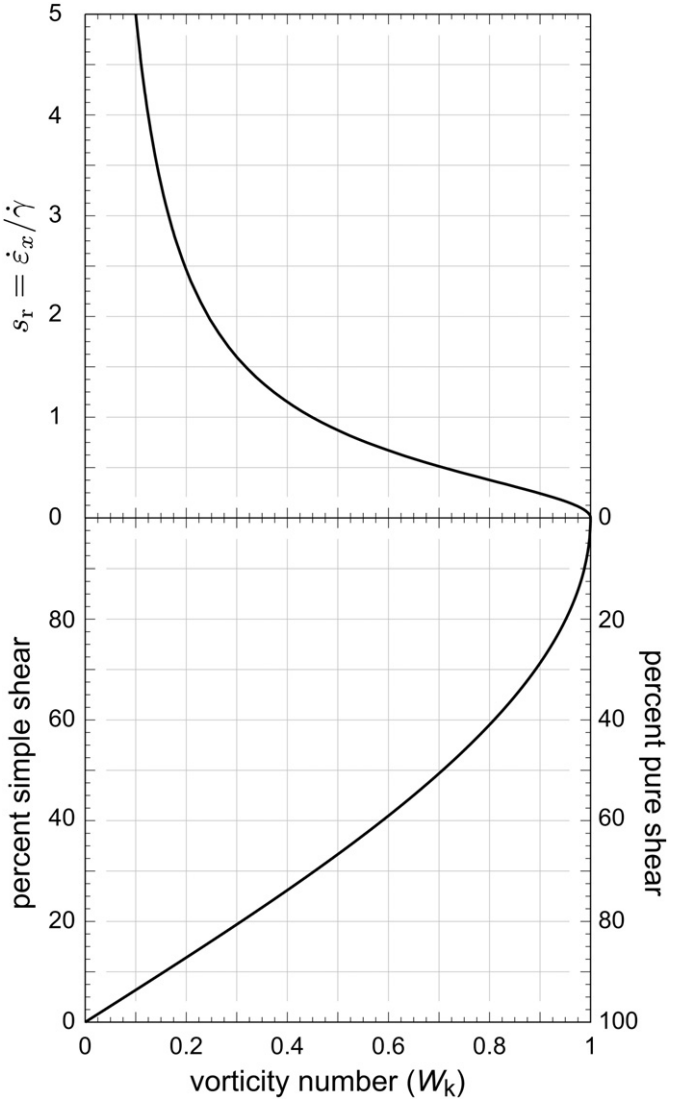

Fig. 2. Variation of percent simple shear and $s_r = \dot{\varepsilon}_x/\dot{\gamma}$ with kinematic vorticity number, W_k. Note both quantities s_r and percent simple shear are moderately to strongly nonlinear for different ranges of W_k. Percent simple shear rapidly increases as W_k approaches unity. Note also the quantity s_r increases without bound as pure shearing end-member is approached.

$$\mathbf{D} = \exp[\mathbf{L}t] = \begin{bmatrix} \exp(\dot{\varepsilon}_x t) & \frac{1}{s_r}\sinh(\dot{\varepsilon}_x t) \\ 0 & \exp(\dot{\varepsilon}_y t) \end{bmatrix} \tag{12}$$

(cf. Ramberg, 1975, Eq. (38); see also Bobyarchick, 1986). It is therefore possible to determine particle paths for any **L** and any choice of kinematic vorticity number.

The finite strain state is also simply related to **D** (and therefore **L**). The tensor, **F** (Finger tensor of Tikoff and Fossen, 1993) contains a complete description of the finite strain accumulated to time t for a given flow. **F** may be obtained from **D** by forming

$$\mathbf{F} = \mathbf{D}\mathbf{D}^T \tag{13}$$

(Malvern, 1969, p. 174) where $\mathbf{D}^T$ is the matrix transpose of **D**. The eigenvalues of **F** give the squares of the semi-axes of the finite strain ellipse and the eigenvectors give their orientations (Tikoff and Fossen, 1993). Thus, by simply choosing appropriate instantaneous strain rates for a particular kinematic vorticity number of interest we may calculate the velocity field and any particle path. We may also determine the finite matrix strain parameters at any time during the flow.

3. Orientation of rigid elliptical objects embedded in a steady viscous flow

3.1. Rotation rate of elliptical clasts

We have chosen to use the angle (θ) between the clast long axis and flow plane in our analysis to reflect a reference frame commonly used in the kinematics literature (cf. Kanagawa, 1996). Here we take the angle as positive if the clast is leaning in the direction of the applied simple shearing component; a dextral shear couple is considered positive (Fig. 3). Clasts rotating counterclockwise in this frame give rise to a positive rotation rate. To accomplish this change of reference frame we substituted the angle $\theta = 90 - \phi$ into the independent variable ϕ in Ghosh and Ramberg's Eqs. (1) and (2).

Upon substitution, the rotation rate for a clast in simple shear becomes

$$\begin{aligned} \dot{\theta}_\gamma &= -\dot{\gamma}\frac{R^2\cos^2(90-\phi) + \sin^2(90-\phi)}{R^2+1} \\ &= -\dot{\gamma}\frac{R^2\sin^2(\theta) + \cos^2(\theta)}{R^2+1}. \end{aligned} \tag{14}$$

The rotation rate for a clast in pure shear flow becomes

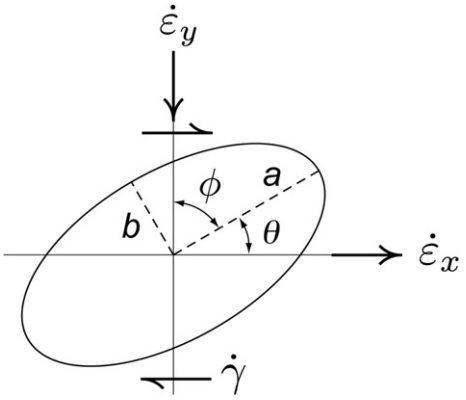

Fig. 3. Kinematic reference frame used in this paper. The angle (θ) between clast long axis and extensional flow apophysis (i.e., flow or shear plane) measured as shown; counterclockwise rotation considered positive. Clast aspect ratio (R) obtained by forming the ratio of long to short semi-axis lengths, $R = a/b$. The angle ϕ was used in the work by Ghosh and Ramberg (1976). Note $\theta = 90 - \phi$.

$$\dot{\theta}_\varepsilon = -\dot{\varepsilon}_x \frac{R^2-1}{R^2+1}\sin[2(90-\phi)] = -\dot{\varepsilon}_x \frac{R^2-1}{R^2+1}\sin(2\theta). \quad (15)$$

Addition of the instantaneous clast rotation rates in pure and simple shear gives the expression for the instantaneous rotation rate of a clast in a general shear flow

$$\dot{\theta} = -\dot{\varepsilon}_x \frac{R^2-1}{R^2+1}\sin(2\theta) - \dot{\gamma}\frac{R^2\sin^2(\theta)+\cos^2(\theta)}{R^2+1}$$

which, after minor manipulation becomes

$$\dot{\theta} = -\dot{\gamma}\left[A\cos^2(\theta) + B\sin(2\theta) + C\sin^2(\theta)\right] \quad (16)$$

where

$$A = \frac{1}{R^2+1}, \quad B = s_r\frac{R^2-1}{R^2+1}, \quad C = \frac{R^2}{R^2+1}.$$

Note the similarity of Eq. (16) to Eq. (4a) of Ghosh and Ramberg (1976).

3.2. Final clast orientation

The relationship between the initial and final angle of a clast suspended in the flow is obtained by integrating the rotation rate Eqs. (14)–(16). The boundary conditions in our analysis are: (1) γ (or ε_x) = 0 and $\theta = \theta_0$ when $t = 0$; and (2) γ (or ε_x) = $\dot{\gamma}t$ (or $\dot{\varepsilon}_x t$) and $\theta = \theta$ when $t = t$ (see also Kanagawa, 1996). Thus, the simple shear component at time t is given by

$$\gamma = \int_{t=0}^{t=t} \dot{\gamma}\mathrm{d}t = \dot{\gamma}t.$$

Similarly, the value of finite pure shear strain at time t is

$$\varepsilon_x = \int_{t=0}^{t=t} \dot{\varepsilon}_x \mathrm{d}t = \dot{\varepsilon}_x t$$

(see also Masuda et al., 1995). Alternatively, using the continuum mechanics notation

$$\gamma = L_{12}t$$

and

$$\varepsilon_x = L_{11}t$$

where $L_{ij}t$ is a component of the velocity gradient tensor multiplied by the temporal duration of deformation. Once the flow type and finite strain to be modeled have been chosen, parameters from the matrix strain may be input into the finite rotation equations given below to determine the orientation of a clast in the flow at any time t (Fig. 4).

3.2.1. Simple shear flow

We may rewrite Eq. (14) and integrate both sides between the boundaries discussed above to obtain

$$-\dot{\gamma}t = \int_{\theta_0}^{\theta} \frac{R^2+1}{R^2\sin^2(\theta)+\cos^2(\theta)}\mathrm{d}\theta. \quad (17)$$

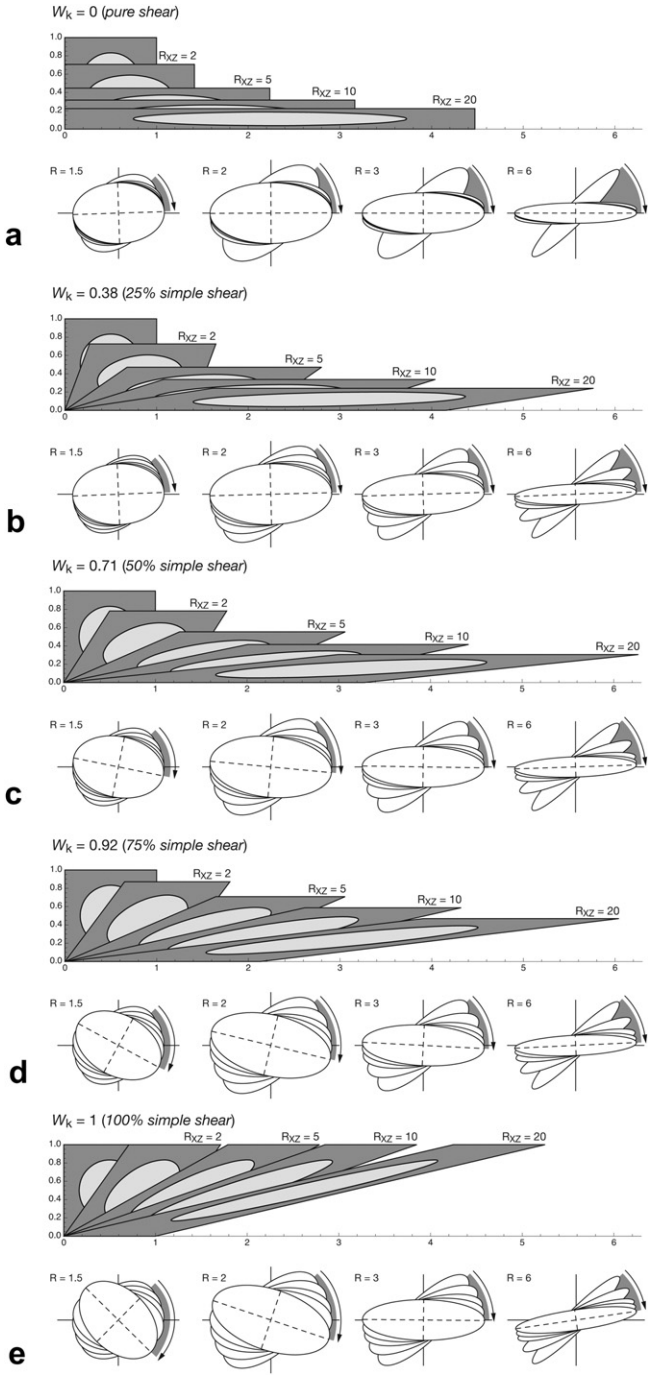

Fig. 4. Orientation of selected individual rigid clasts suspended in a Newtonian matrix during progressive deformation. Dark gray boxes show initially square matrix element deformed to strain ratios of $R_{XZ} = 2$, 5, 10, and 20. Passive circular markers deformed into finite strain ellipses indicated by lighter gray screen at each deformation stage. Abscissa and ordinate scales equal. Shown below strained matrix elements are orientations of rigid clasts (no pattern) of aspect ratio $R = 1.5$, 2, 3, and 6 embedded in the matrix at the given R_{XZ} values (all clasts had +45 degrees initial orientation). Dashed lines indicate trace of clast semi-axes after last deformation increment. Arrows indicate sense and approximate amount of clast rotation. (a) Pure shear. (b) $W_k = 0.38$ (25% simple shear). (c) $W_k = 0.71$ (50% simple shear). (d) $W_k = 0.92$ (75% simple shear). (e) Simple shear. Note rapidly increasing shear zone-parallel stretch for flows with higher pure shearing component. Rotation amounts of suspended clasts generally decrease with increasing R for a given flow, while the finite rotation angle increases for constant low aspect ratio clasts for flows of increasing W_k (this trend reverses for higher aspect ratio clasts). See text for discussion.

Upon integration and solving for the final orientation θ, we obtain

$$\theta = \tan^{-1}\left[\frac{1}{R}\tan\left\{\tan^{-1}(R\tan\theta_0) - \dot{\gamma}t\frac{R^2}{R^2+1}\right\}\right] \quad (18)$$

where θ_0 is the initial orientation of the long axis of the elliptical inclusion.

3.2.2. Pure shear flow

Similarly, we may rewrite Eq. (15) and integrate both sides, such that

$$-\dot{\varepsilon}t = \frac{R^2+1}{R^2-1}\int_{\theta_0}^{\theta}\frac{\mathrm{d}\theta}{\sin(2\theta)}. \quad (19)$$

Upon integration and solving for the final orientation θ, we obtain

$$\theta = \tan^{-1}\left[\tan(\theta_0)\cdot\exp\left(-2\dot{\varepsilon}t\frac{R^2-1}{R^2+1}\right)\right]. \quad (20)$$

3.2.3. General shear flow

Finally, we may rewrite Eq. (16) and integrate both sides, such that

$$-\dot{\gamma}t = \int_{\theta_0}^{\theta}\frac{\mathrm{d}\theta}{A\cos^2(\theta)+B\sin(2\theta)+C\sin^2(\theta)} \quad (21)$$

(cf. Ghosh and Ramberg, 1976, Eq. (10)). The integral on the right hand side of (21) has three types of solution depending on whether $B^2 > AC$, $B^2 < AC$ or $B_2 = AC$. The solutions to these integrals may be found in any book of standard mathematical tables. Upon integration, the solutions for θ for each case are (see also Ghosh and Ramberg, 1976):

1. $B^2 > AC$:

$$\theta = \tan^{-1}\left[\frac{P\left(B+\sqrt{B^2-AC}\right)-B+\sqrt{B^2-AC}}{C(1-P)}\right] \quad (22)$$

where

$$P = \frac{C\tan(\theta_0)+B-\sqrt{B^2-AC}}{C\tan(\theta_0)+B+\sqrt{B^2-AC}}\cdot\exp\left[-2\dot{\gamma}t\sqrt{B^2-AC}\right]$$

2. $B^2 < AC$:

$$\theta = \tan^{-1}\left[\frac{\sqrt{AC-B^2}}{C}\times\tan\left\{\tan^{-1}\left(\frac{C\tan(\theta_0)+B}{\sqrt{AC-B^2}}\right) - \dot{\gamma}t\sqrt{AC-B^2}\right\} - \frac{B}{C}\right] \quad (23)$$

3. $B^2 = AC$:

$$\theta = \tan^{-1}\left[\frac{1}{C}\left\{\frac{C\tan(\theta_0)+B}{1+\dot{\gamma}t(C\tan(\theta_0)+B)} - B\right\}\right]. \quad (24)$$

4. Review of inclusion and passive marker re-orientation in a steady flow

The behavior of individual elliptical and passive line elements in a flowing matrix is critical to understanding the behavior of the larger populations of non-interacting elliptical inclusions that we will discuss throughout the remainder of this paper. Here we briefly review basic properties of the behavior of elements embedded in selected steady flows. Because our model uses the governing equations of Ghosh and Ramberg (1976) the assumptions built into their formulation apply here as well. Namely, we assume: (1) clasts are rigid, elliptical, and are embedded in a linear viscous (i.e., Newtonian) matrix; (2) one symmetry axis of the clast is parallel to the vorticity vector; (3) the flow is steady, with a simultaneous combination of pure and simple shearing; and (4) perfect coupling of the clast and matrix.

4.1. Rotation rate of rigid inclusions

In this section we present plots of rate of change of orientation ($\dot{\theta}$) divided by strain rate ($\dot{\varepsilon}_x$ or $\dot{\gamma}$, as appropriate) vs. orientation (θ) of clast long axis. These plots may be thought of as a normalized rotation rate vs. orientation in the flow. The fundamental behavior of rigid particles suspended in a flowing viscous matrix that forms the basis of clast-based vorticity gauges is depicted in these plots. Therefore, considerable attention is devoted to unique aspects of the behavior of clasts in simple shear, pure shear, and mixed flow type.

4.1.1. Simple shear flow

Patterns of rotation rate in a simple shear flow are by far the simplest (Fig. 5a). All inclusions rotate synthetic to the imposed shear direction with the exception of a passive line element parallel to the shear plane, which has zero angular velocity. A spherical inclusion rotates at half the applied shear strain rate. Line elements and large aspect ratio (R) grains have lower angular velocities within ±45 degrees of the flow plane, and higher angular velocities at any other orientation. Rotation rates are a maximum for an inclusion of any aspect ratio when it is at high angles to the flow plane, and minimum when parallel. Note that all elliptical or linear elements embedded in the matrix have identical angular velocities when they are at exactly ±45 degrees to the flow plane (i.e., when they are parallel to the ISA). This is a general feature of suspended clasts in any flow type.

4.1.2. Pure shear flow

Rotation rates of elliptical objects suspended in a pure shear flow are more complex than those in simple shear flow (Fig. 5b). Spherical clasts do not rotate, whereas positive and negative rotation rates (i.e., counterclockwise and clockwise rotation, respectively) are predicted for all elongate clasts, depending on orientation. Maximum absolute values of rotation rates are obtained for any non-spherical clast at ±45 degrees to the flattening plane. Grains of higher R always have faster rotation rates (either positive or negative) than grains of lower R in the same orientation.

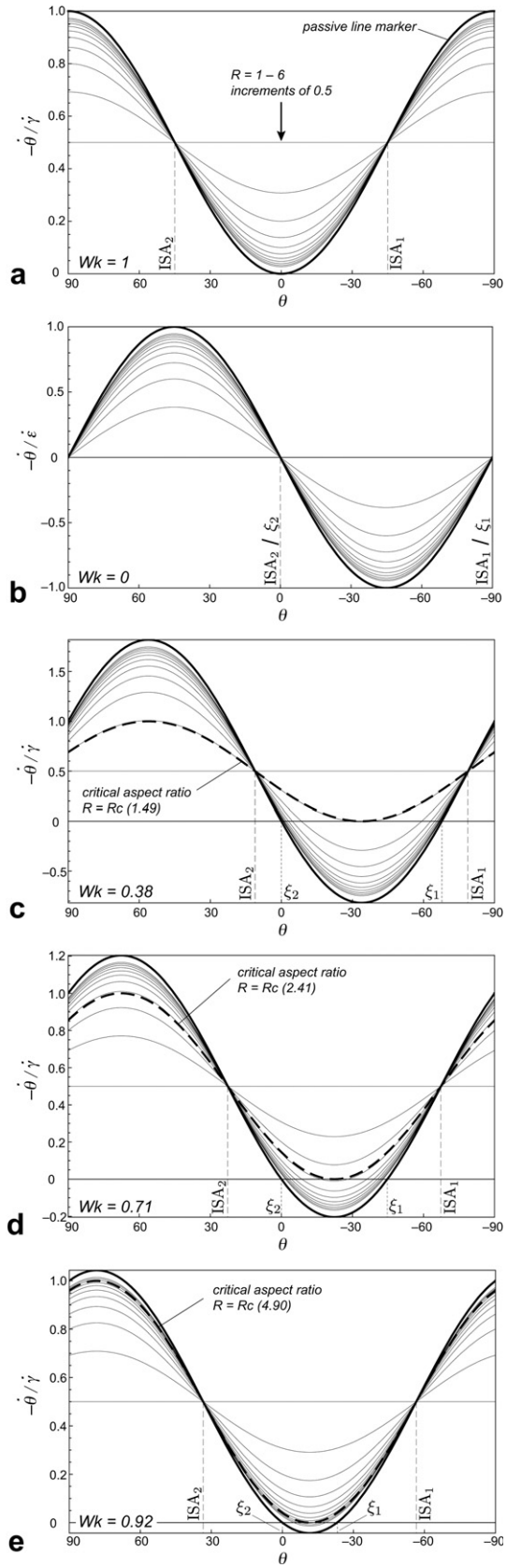

Fig. 5. Normalized rotation rate vs. clast orientation plots for elements embedded in a viscous flow. (a) Simple shear. (b) Pure shear. (c) $W_k = 0.38$ (25% simple shear). (d) $W_k = 0.71$ (50% simple shear). (e) $W_k = 0.92$ (75% simple shear). Thin curves represent clasts with aspect ratios ranging from 1 to 6 in increments of 0.5 (i.e., $R = 1, 1.5, 2, \ldots, 6$); labels omitted for clarity. Thick solid curve represents a passive line marker, thick dashed curve (c–e) represents clast with $R = R_{crit}$. Passive line markers and clasts (regardless of aspect ratio) have identical angular velocity when parallel to ISA of the flow. Clasts with aspect ratios $R > 5$ approximate behavior of passive line elements. ISA_i and ξ_i indicated by dashed and dotted lines, respectively. Note clasts with $R \approx R_{crit}$ have rotation rates that are such a small fraction of the applied shear strain rate when in orientations near the flow plane that they may be mistaken for clasts with a stable orientation. Compare Figs. 9–11. See text for discussion.

Inclusions and linear elements parallel and perpendicular to the flattening plane (parallel to ISA) have zero angular velocity.

4.1.3. General shear flow

Clasts embedded in a matrix undergoing general shear share attributes with those in both pure and simple shear flow; however, the most significant feature is the existence of a particular aspect ratio whose rotation rate vanishes in a flow of a given vorticity (Fig. 5c–e). This aspect ratio is termed the *critical aspect ratio*, R_{crit}. Clasts with $R < R_{crit}$ rotate synthetic to the imposed simple shearing component only, whereas those with $R > R_{crit}$ have fields of positive and negative rotation rate. Each clast with $R > R_{crit}$ has one stable and one metastable orientation in the flow. A clast initially in a metastable orientation, after any perturbation, will rotate toward its stable orientation (i.e., the stable orientation at a lower angle to the flow plane). The value of R_{crit} increases with increasing vorticity number until, in the limit, $R_{crit} = \infty$ for simple shear flow. Because R_{crit} is unique for a given general shear flow, the kinematic vorticity may theoretically be calculated if this aspect ratio can be determined (Fig. 6).

4.2. Field of back-rotation

The existence of both negative and positive angular velocities for flows with $0 < W_k < 1$ discussed above indicate that some clasts will rotate *against* the applied shear direction during sub-simple shearing. In fact, Fig. 5c–e clearly indicates the range of orientations for which a clast may back-rotate is a function of aspect ratio and kinematic vorticity. Clasts with R only slightly greater than R_{crit} have a more restricted range of orientations where back-rotation is possible than clasts with $R \gg R_{crit}$. In the limit, passive line elements define the widest possible orientation range for back-rotation in a given flow. The orientation where curves representing passive line markers intersect the zero angular velocity contour are by definition the orientation of the flow apophyses (i.e., eigenvectors, ξ_i, of the velocity gradient tensor, $\mathbf{L}$). These orientations separate fields of forward and backward rotation for a given flow. It can also be seen that the single stable orientation for clasts with $R = R_{crit}$ bisects the acute angle between the eigenvectors of $\mathbf{L}$. The size of the field of back-rotation increases rapidly with increasing aspect ratio (Fig. 5c–e).

5. Kinematic model

5.1. Initial and boundary conditions

In an attempt to model as realistic a clast population as possible, we combined observations from 76 mylonitic samples (total of 14,959 measured porphyroclasts) from a variety of lithologies and tectonic settings (Fig. 7a–c). Our model utilizes a large population of clasts ($n = 500$) with aspect ratios satisfying the requirement $1 \leq R \leq 7$, in the same proportions as our combined dataset (i.e., the histogram of model clasts is identical to that in Fig. 7d, but the total data sum to $n = 500$). Initial orientations (θ_0) for our clasts ranged from −90 to +90 degrees and were derived using a random number generator so every possible pair of R and θ_0 values from the range given above is well-represented in the initial population (Fig. 8).

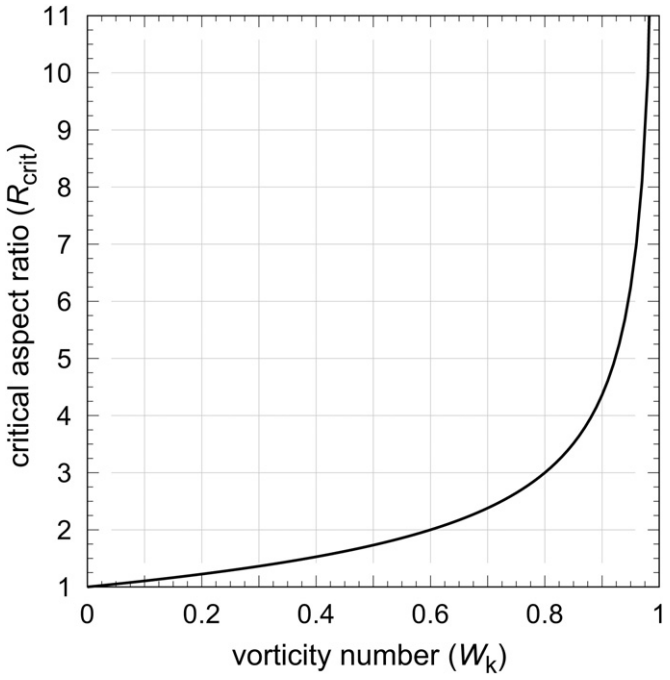

Fig. 6. Relationship between critical aspect ratio (R_{crit}), and kinematic vorticity number (W_k). R_{crit} increases only from 1 to 2 for an increase in W_k of 0–0.6 (i.e., an increase from 0 to 40% simple shearing component). The ability to accurately distinguish flows with R_{crit} in this range may be difficult for natural mylonites. Note also R_{crit} increases rapidly and without bound for kinematic vorticity values above $W_k \approx 0.9$.

The same initial population was used to calculate the orientation distribution at each finite strain state for each flow.

We modeled flows with W_k values of 0 (pure shear), 0.38 (25% simple shear), 0.71 (50% simple shear), 0.92 (75% simple shear), and 1 (100% simple shear) to investigate the effects of increasing simple shearing component on clast orientation distributions. The orientation distributions shown here were calculated for matrix strain ratios (R_{XZ}) of 2, 5, 10, 20, 50, 100, 200, and 500. Animations depicting the evolution of clast orientation distributions during progressive deformation for all five model flows presented in this paper are provided as an electronic supplement.

5.2. Results

It is apparent from our model results that moderate to high finite strains are required for clasts with $R \geq R_{crit}$ to rotate into their stable orientation (Fig. 9). However, due to the different response of clasts of variable aspect ratio to the imposed boundary conditions, not all clasts above R_{crit} reach the flow plane after an identical matrix strain, so a well-developed clast orientation distribution is not developed for each flow after the same duration of deformation. In other words, flows of different vorticity require different amounts of finite strain to produce well-organized porphyroclast orientation distribution patterns that will yield reliable results from the rigid grain technique.

The final orientation, or finite angle of rotation, of a clast is a complex function of aspect ratio, initial orientation, flow vorticity, and finite strain. Fig. 4 provides insight into the behavior of a small subset of grains within the larger population used to calculate clast

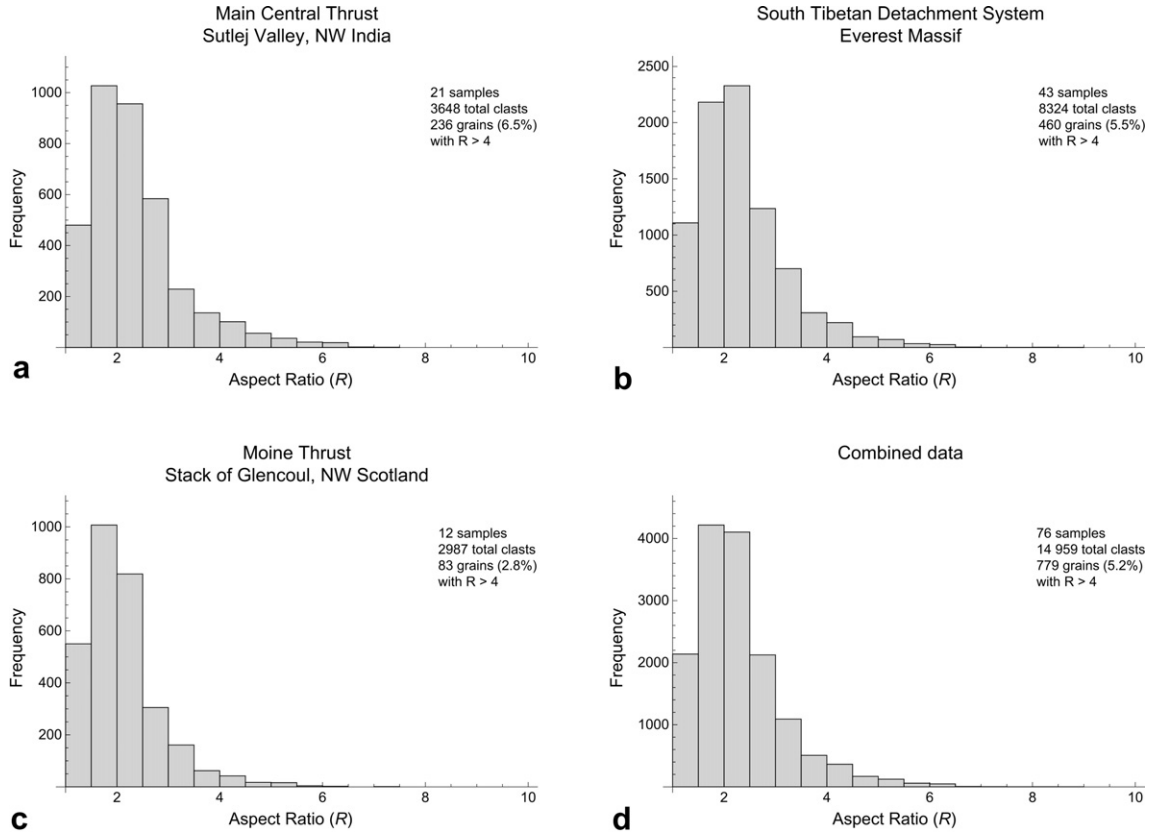

Fig. 7. Histograms showing frequency of clast aspect ratios measured in natural mylonites. (a) Results from examination of 21 mylonitic samples (3648 total clasts) from the Main Central Thrust zone, Sutlej Valley, NW India (unpublished data). (b) Results from examination of 43 mylonitic samples (8324 total clasts) from the South Tibetan Detachment System, Everest Massif (Jessup et al., 2006). (c) Results from examination of 12 mylonitic samples (2987 total clasts) from the Moine Thrust, Stack of Glencoul, NW Scotland (Law, 2010). (d) Results of combined datasets. Note grains with $R \leq 3$ dominate the natural populations, but clasts with $R \geq 4$ are much less common (here they represent between only ~3 and 6.5% of the population for a given dataset, and ~5% of the total data).

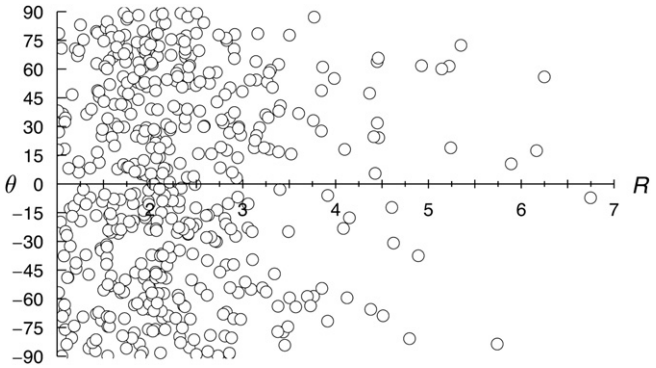

Fig. 8. Initial population. Clast aspect ratios (R) range from 1 to 7, and initial angles (θ_0) range from −90 to +90 degrees. Clast proportions of total population are as detailed for combined natural datasets (Fig. 7d). Pairs (R, θ_0) chosen using a random number generator to represent a homogeneous distribution of clast initial orientations.

orientation distributions. An initial square matrix element with embedded passive circular marker is shown in the initial configuration and after matrix strains of $R_{XZ} = 2$, 5, 10, and 20 for each modeled flow. Progressive deformation may be monitored by change in angles or calculated directly by measuring the passive strain ellipse. Shown below the graphical matrix strains in Fig. 4 are rigid elliptical clasts of variable aspect ratio ($R = 1.5$, 2, 3, and 6), all initially at +45 degrees to the flow plane, and their orientation after each matrix strain increment. The figure clearly shows the maximum angle of finite rotation is ~90 degrees for a grain with $R = 1.5$ and a matrix strain of $R_{XZ} = 20$ in a simple shear flow. All other grains in pure and general shear rotate significantly less after identical matrix strains. This is the case if the clast aspect ratio is well above, below, or near R_{crit} for the flow. Also evident from the figure is a decrease in rotation angle with increasing strain when clast long axes approach parallelism with the flow plane. Most clasts in these examples rotate no more than ~20 degrees during progressive matrix strains of 5–20. This is an important point that has implications for clast orientation distributions at high finite strain.

5.3. Clast orientation distributions at high finite strain

An interesting phenomenon occurs in the models for high W_k flows at moderate to high finite strains (e.g., $W_k = 0.92$ flow at $R_{XZ} > 10$; Fig. 9). Clasts with $R < R_{crit}$ rotate into sub-parallelism with the flow plane and remain near this orientation until very high strains accumulate. Similar results are obtained for all flows, but the phenomenon becomes increasingly apparent for higher W_k flows simply because a similar percentage of R_{crit} occupies a larger R range.

For the case of the $W_k = 0.92$ flow, clasts with $R \geq 4.4$ (within approximately 10% of $R_{crit} = 4.9$) reach sub-parallelism with the extensional flow apophysis and remain near this position regardless of their initial orientation (Fig. 10). These clasts do not become significantly re-oriented until matrix strains of $R_{XZ} \approx 275{,}000$ ($\dot{\gamma}t \approx 25$), and even then nearly all clasts in this range are predicted to lie within 20 degrees of the flow plane. Thus, for geologically realistic and greater matrix strain ratios, clasts within this range are indistinguishable from grains with $R \geq R_{crit}$; they are effectively stable. If we now examine clasts further separated from R_{crit}, say within ~22 to 10% (i.e., $3.8 \leq R \leq 4.3$), we see the behavior is similar but less pronounced (Fig. 11). Here the lower aspect ratio clasts rotate to greater (negative) angles to the flow apophysis by the time we reach the maximum strains modeled, on the order of $R_{XZ} = 500$. Therefore, by the time moderate strains are reached in this flow, nearly all clasts within ~22% of R_{crit} have rotated to within ~10 degrees of the flow plane and will remain close to this orientation until large finite strains accumulate.

The reason for this behavior is clearly seen in the rotation rate vs. orientation curves (Fig. 5c–e). The normalized rotation rate of clasts with R near R_{crit} is such a small fraction of the applied shear strain rate, particularly in orientations near the extensional flow apophysis, that very high shear strains are necessary for clasts to rotate away from the flow plane (cf. Marques and Coelho, 2003).

6. Discussion

6.1. Model predictions

The numerical model presented here of evolving clast orientation distributions for steady flows of variable vorticity provides insight into the first-order behavior of natural systems during progressive deformation. The model allows direct comparison of the effects of progressive deformation for a steady flow and of increasing simple shearing component for viscous flows at constant strain states. Our results confirm previous conclusions (Masuda et al., 1995; Bailey et al., 2007; Mulchrone, 2007) that clast-based kinematic vorticity gauges may aid in discriminating pure and simple shear-dominated flows. We also found that large clast populations with a large range of clast aspect ratios are required for a reliable estimate of R_{crit}. This point has received little attention in the recent literature and will be discussed further below.

6.1.1. Pure shear-dominated flows

Our results indicate rather high strains are required to identify low W_k flows due to the relatively slow rotation of clasts with $R \geq 2$, particularly when they have initial orientations at moderate to high negative angles to the flow plane. Even in these strongly pure shear-dominated flows, relatively high strains (e.g., $1 \leq \dot{\gamma}t \leq 2$) are required to rotate clasts above R_{crit} into their stable orientations subparallel to the flow plane (see e.g., Ghosh and Ramberg, 1976, their Figs. 9–13). For the modeled pure shear flow, elongate clasts tend to reach the flattening (foliation) plane at the lowest R_{XZ} values, but finite strains on the order of >20:1 appear necessary for the majority of clasts to reach their stable orientation. Similarly, visual estimates of R_{crit} for the $W_k = 0.38$ flow tend to produce an overestimate of the applied vorticity for all modeled strain states (Fig. 9). Visually estimated R_{crit} for this flow appears to lie between 2 and 3 for much of the deformation history, even for strain ratios approaching 500:1. This may be one contributing factor to the $W_k = 0.65$–0.75 results obtained from samples interpreted to have experienced pure shear-dominated flow (e.g., Bailey et al., 2007).

6.1.2. Simple shear-dominated flows

Clast orientation distributions closely resembling those expected for lower W_k flows are predicted for high W_k flows, even at low finite strain (Fig. 9). Here clasts of all aspect ratios rotate slowly in orientations subparallel to the flow plane so high strains must accumulate to rotate these grains from this orientation. Greater strains are needed for higher aspect ratio clasts, even though they are unstable in the flow (Figs. 9–11).

The visually estimated R_{crit} of the $W_k = 0.92$ flow model at high strain ($R_{XZ} > 20$) is ~3 to 3.75, corresponding to a W_k of 0.8–0.87 (Fig. 9). This is a significant underestimation of the simple shearing component of flow (16–8%). The lower bound on visual estimates of the $W_k = 0.71$ flow may also yield underestimates on the applied vorticity of the same order (~10%) at high strain. Notice that this range of visually estimated W_k values is in agreement with results reported from many studies, even if higher W_k estimates were

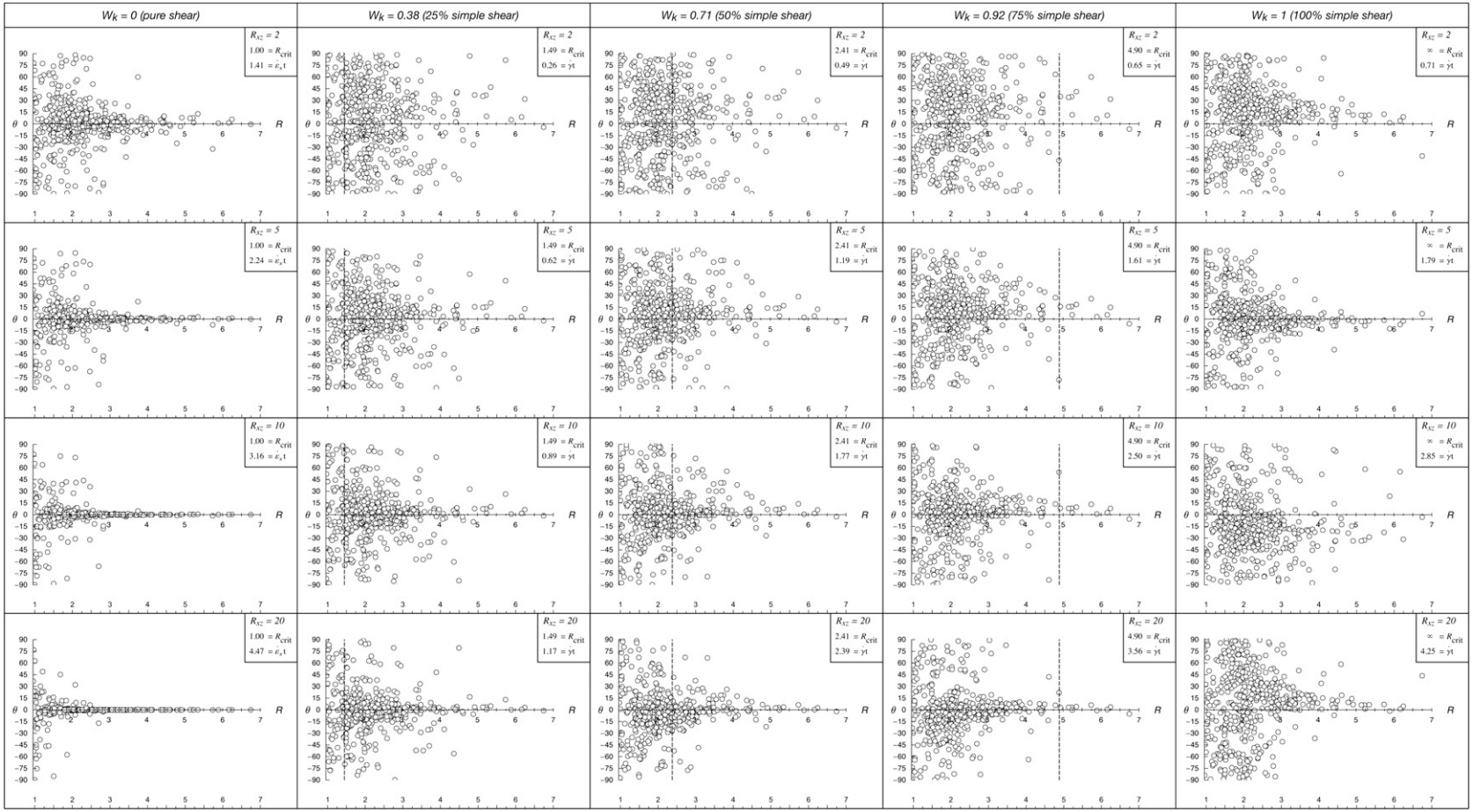

Fig. 9. Kinematic model results for five steady flows (W_k=0, 0.38, 0.71, 0.92, and 1) at eight different finite strain ratios (R_{XZ} = 2, 5, 10, 20, 50, 100, 200, and 500). Constant W_k values aligned in columns; rows contain results from different W_k values calculated at identical matrix strain ratios. Dashed vertical lines indicate theoretical R_{crit} for given flow. Finite matrix strain, R_{XZ}, theoretical critical aspect ratio, R_{crit}, and strain component, $\varepsilon = \dot{\varepsilon}_x t$ or $\gamma = \dot{\gamma} t$, used to produce orientation distribution indicated.

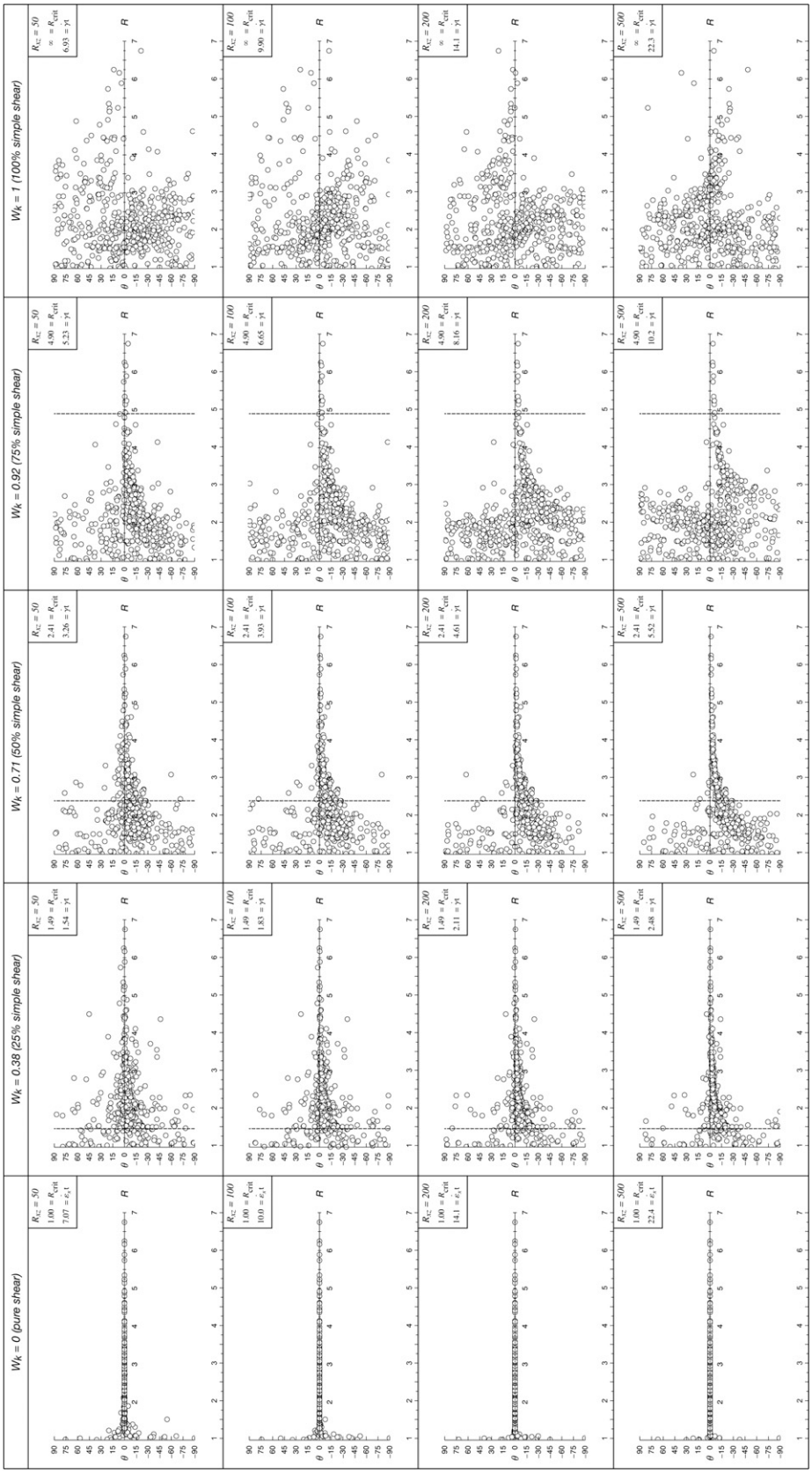

Fig. 9. (*continued*).

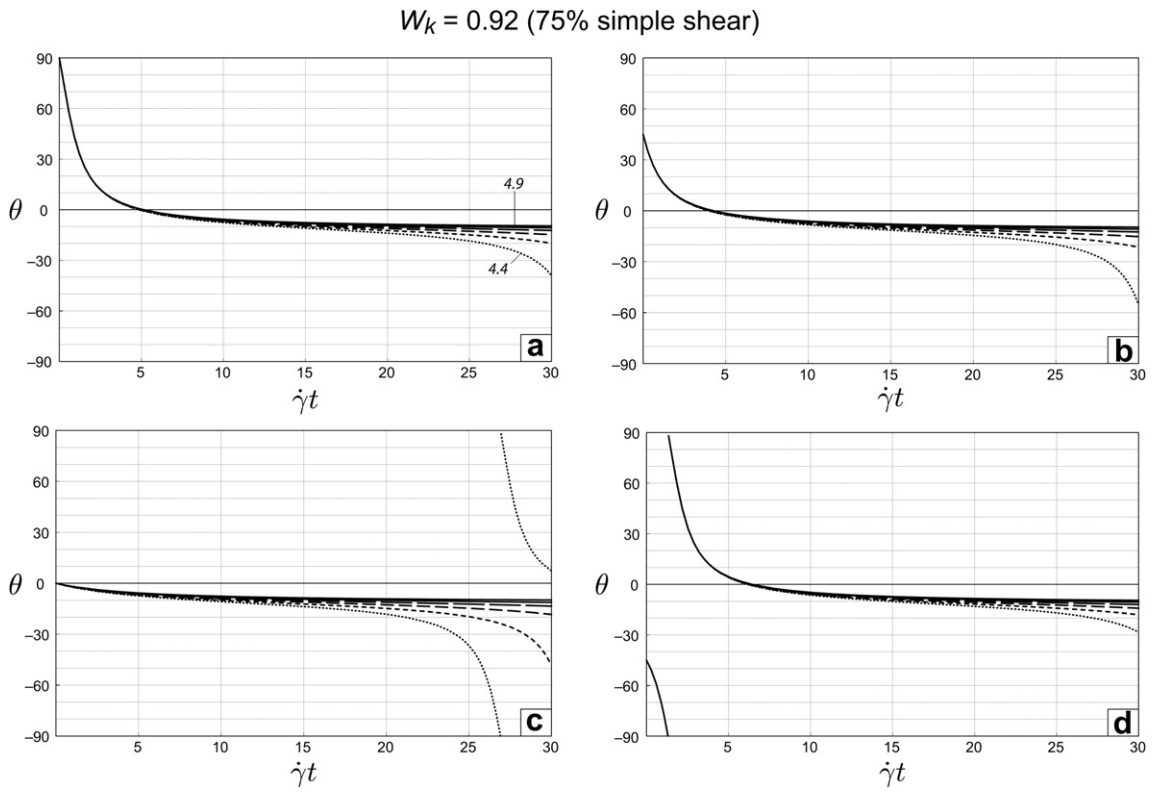

Fig. 10. Orientation (θ) of clast long axis (cf. Fig. 3) vs. simple shear component ($\dot{\gamma}t$) for a flow of $W_k = 0.92$. Aspect ratios of $R = 4.4, 4.5, \ldots, 4.9$ shown (i.e., clasts within ~10% of R_{crit}). Length of dashes in pattern increase with increasing R; some labels omitted for clarity. Initial clast orientations of (a) +90 degrees, (b) +45 degrees, (c) 0 degrees, and (d) −45degrees.

obtained for the same samples using different methods. We suspect that pseudostable behavior of clasts with $R < R_{crit}$, particularly in simple shear-dominated flows, may be another potential cause of the ubiquitous 0.65–0.75 W_k estimates from natural rocks. Underestimations of the simple shearing component of the magnitude estimated here, propagated through calculations of shear zone-parallel stretch, may yield substantial errors that impact interpretations relating the role of general shear flow to deformation-driven exhumation of plastically deformed rocks.

6.2. Application to naturally deformed rocks

Clearly, a critically important factor regarding the reliability of the rigid grain technique is the existence of a population of grains with $R > R_{crit}$. For example, samples must have a population of grains with $R > 3$ for effective discrimination of flows with $W_k > 0.8$ (Fig. 6). Results from our own analyses, complimented by a brief examination of published analyses (e.g., Xypolias and Koukouvelas, 2001; Law et al., 2004; Jessup et al., 2006; Jessup et al., 2007; Bailey et al., 2007; Johnson et al., 2009; Thigpen et al., 2010), unfortunately reveal that many natural rocks lack a significant population of suitable grains to discriminate high vorticity flows. For example, examination of the 76 mylonitic rocks from which we derived the aspect ratio distribution for our initial population, revealed that approximately 5% (779 of 14 959 clasts) have aspect ratios greater than $R = 4$ (Fig. 7). This value is consistent with other published studies. Such a small fraction of high aspect ratio grains in naturally deformed rocks indicates that flows with more than ~60 to 70% simple shearing component are not generally identifiable by the rigid grain method.

We suggest that a lack of high aspect ratio grains may be yet another contributing factor to the overwhelming 0.65–0.75 W_k estimates for naturally deformed rocks obtained from clast-based techniques. Our experience suggests that for natural samples, clasts with $R < 3$ are abundant while grains with $R > 4$ are much more uncommon. Uncritical use of such naturally limited datasets will tend to produce underestimates of W_k for natural mylonites (assuming they experience moderate to high vortical flows). We suspect that it is unrealistic to expect to identify flows with $W_k > 0.85$, and discriminating flows with this high of a simple shearing component is likely only possible under ideal circumstances.

6.2.1. Example

We present a brief example illustrating some limitations of the rigid grain technique by examining in more detail samples from the Rongbuk valley, Everest massif, originally presented by Law et al. (2004). We are primarily interested in the influence variable matrix strains and variable vorticity values have on the theoretical orientation distribution of porphyroclasts. We will examine the impact of finite strain estimates that vary over two orders of magnitude ($R_{XZ} \sim 2$–250). Both the rigid grain and R_{XZ}/β techniques have been applied to several of the same samples (see Law et al., 2004, Table 1, samples ET08 and ET12–ET14). Rigid grain analyses applied to these rocks resulted in W_m estimates in the range of 0.67–0.85 (mean of 0.76). Here we use the notation W_m to indicate the measured vorticity was not likely an instantaneous quantity. Application of the R_{XZ}/β method to the same rocks, however, yielded W_m estimates in the range 0.78–0.94 (mean of 0.87), providing an upper bound on flow vorticity during mylonitization. We will show that this vorticity range is indistinguishable

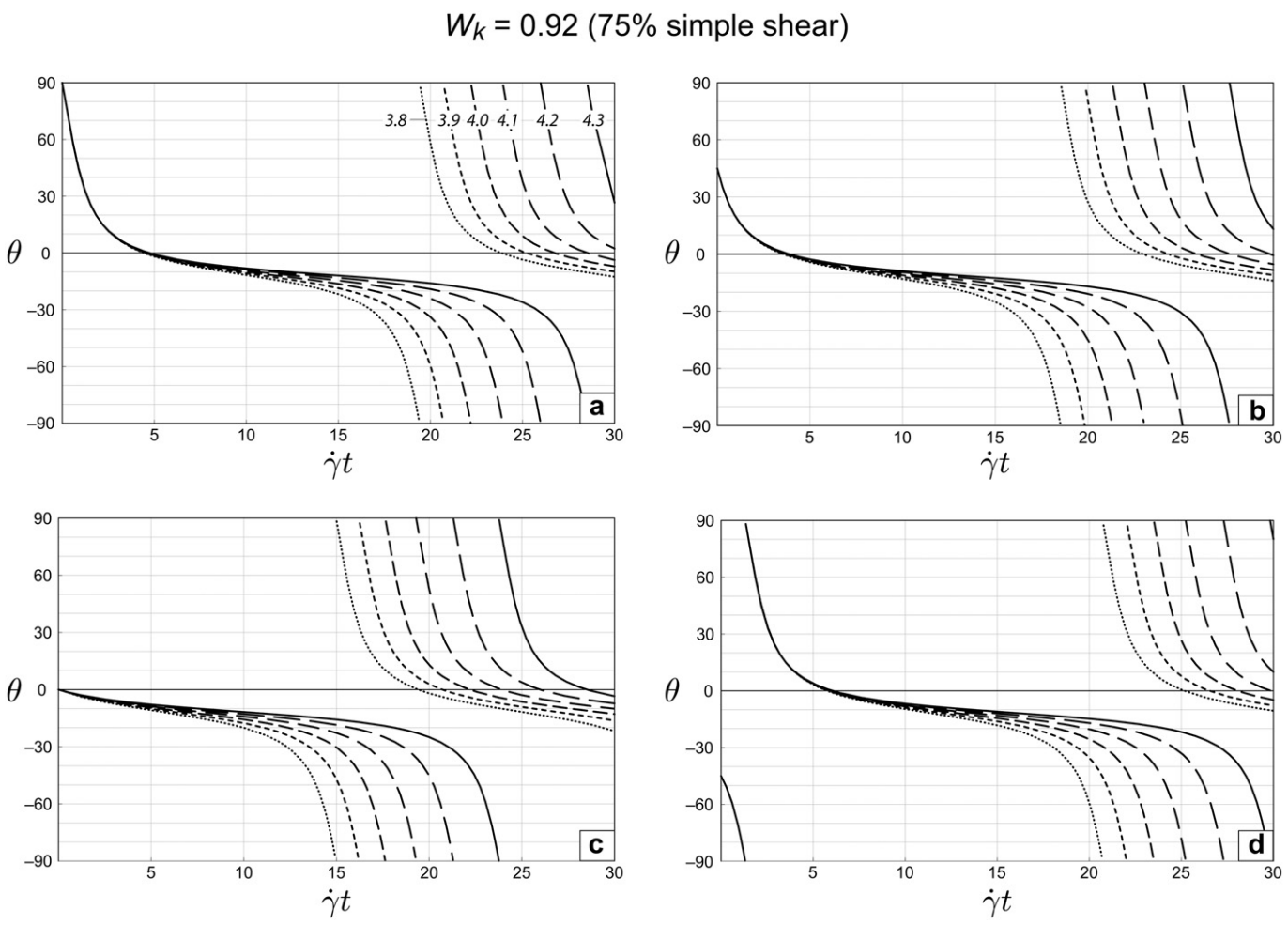

Fig. 11. Orientation (θ) of clast long axis (cf. Fig. 3) vs. simple shear component ($\dot{\gamma}t$) for a flow of $W_k = 0.92$. Aspect ratios of $R = 3.8, 3.9, \ldots, 4.3$ shown (i.e., clasts within ~22 to 10% of R_{crit}). Length of dashes in pattern increase with increasing R. Initial clast orientations of (a) +90 degrees, (b) +45 degrees, (c) 0 degrees, and (d) −45 degrees.

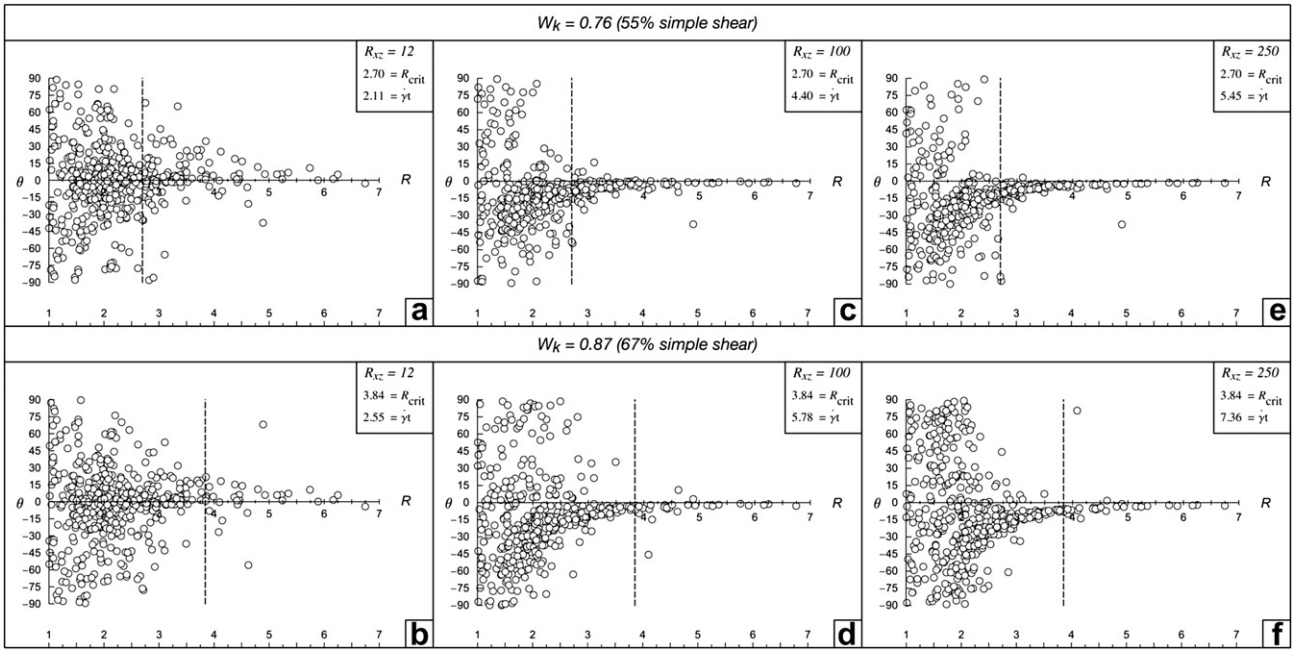

Fig. 12. Model simulations of our original initial clast population for W_k values of 0.76 (upper panel) and 0.87 (lower panel) at matrix strains of (a, b) 12:1, (c, d) 100:1, and (e, f) 250:1. Note that clast orientation distributions are strikingly similar at the same matrix strains for these different W_k values. Thus, the $W_k = 0.76$ value obtained from measurements of the natural mylonites is a likely lower bound on the true flow vorticity, while higher W_k values for these rocks are also possible.

by the rigid grain method, and that large differences in kinematics of simple shear-dominated flows are predicted to be difficult to distinguish using rigid grain analysis.

Minimum strains for these rocks of $R_{XZ} \approx 2-3$ have been inferred from aspect ratios of dynamically recrystallized quartz aggregates surrounded by mica films (Law et al., 2004). At these low matrix strains most grains above R_{crit} have not rotated into their stable orientations (cf. predictions for all flows at similar strains in Fig. 9). It is not until matrix strains of ~10 to 12 that clast populations resembling those observed begin to emerge from our model (Fig. 12a and b). Interestingly, matrix strains of this magnitude are near the maximum compatible with constraints on angle β determined from optically measured quartz c-axis fabrics on reconnaissance samples published by Law et al. (2004). Even at these moderate strain values, however, predictions for the $W_k = 0.76$ flow suggest that the 'true' vorticity may be overestimated in at least some natural rocks. Perhaps more important here than potential W_k underestimates is the similarity of the orientation distributions predicted for both $W_k = 0.76$ and $W_k = 0.87$ flows for a matrix strain ratio of 12:1 (Fig. 12a and b). At R_{XZ} values of 100–250, maximum estimates obtained by assuming a penetrative vertical telescoping of isotherms below the South Tibetan Detachment, clasts with $R \geq R_{crit}$ have rotated into positions approaching their stable orientation. However, even at these high strains the visual estimates of R_{crit} have not changed significantly and both flows modeled are predicted to produce virtually indistinguishable results (Fig. 12c–f).

The important observations here are: (1) for simple shear-dominated flows such as this, finite strain ratios greater than ~10:1 appear necessary for clasts with $R \geq R_{crit}$ to closely approach their stable orientation. At lower matrix strains the rigid grain technique may overestimate the applied vorticity; and (2) similar clast orientation distributions are predicted for significantly different flows at matrix strains higher than $R_{XZ} \approx 10$. Thus, it appears that for simple shear-dominated flows – such as described for the Rongbuk valley – that by the time clasts rotate to near their stable position for moderate vorticity flows (e.g., $W_k \approx 0.7$ or so), strikingly similar orientation distributions are predicted for significantly higher vorticity flows (e.g., $W_k \geq 0.85$). There does not seem to be a way, solely by rigid grain analysis, to identify any flow of significantly greater vorticity than $W_k = 0.65–0.75$, even though grains with $R \geq R_{crit}$ exist in the rocks.

This example underscores the importance of applying multiple techniques to single appropriate samples, and of obtaining independent finite strain estimates for samples selected for rigid grain analysis to determine likely upper and lower bounds on flow vorticity. By combining different vorticity estimation techniques with strain data the two vorticity values estimated for the Rongbuk section are seen to be identical within the limitations of the rigid grain method, rather than incompatible.

7. Conclusions

Our numerical model employing Ghosh and Ramberg's (1976) analytic solutions for the re-orientation of ellipsoidal clasts suspended in a flowing Newtonian matrix indicate: (1) moderate to high matrix strains are required for clasts with $R \geq R_{crit}$ to rotate into their stable orientations – even for flows of low W_k. We cannot state a particular strain ratio that must be attained by a deformed rock to ensure successful application of the technique, however, because different flow types require different matrix strains for clasts with $R \geq R_{crit}$ to approach their stable orientation; (2) in simple shear-dominated flows, some clasts with $R < R_{crit}$ rotate into sub-parallelism with the flow plane and remain near this orientation until large matrix strains accumulate. The exact amount of strain required to re-orient these psuedostable clasts is a function of their aspect ratio and flow vorticity; and (3) although the rigid grain technique may potentially discriminate pure and simple shear-dominated strain paths, the restricted R range of natural clast populations and pseudostable behavior of clasts that exist in many rocks, limit the usefulness of the method for extracting high-quality, meaningful results for many flows, particularly when used as the sole vorticity estimation technique.

We suggest the main limitations regarding application of the rigid grain technique to natural rocks are: (1) a significant population of grains with $R > R_{crit}$ must exist in the sample for it to be useful; (2) high matrix strains must be reached, even in low W_k flows, for clasts to reach their stable orientation. This may cause overestimations of the applied vorticity for many low strain rocks; and (3) at high matrix strains, clast populations in moderate to high W_k flows tend to develop shape preferred orientations that closely resemble those expected for lower W_k flows. The first point is critical because there is no way to know, *a priori*, the kinematic parameters of an ancient flow – indeed, these are the data sought. If the clast population used to extract these parameters is inadequate the results will be biased. The second and third points may provide some insight into the ubiquitous 0.65–0.75 W_k values obtained from natural samples.

In many cases where the quartz *c*-axis fabric and rigid grain methods have been applied to the same sample the results are markedly different. Results obtained from the quartz *c*-axis fabric method often yield $W_k \geq 0.9$, whereas rigid grain results are significantly lower (e.g., Law et al., 2004; Sullivan, 2008; Johnson et al., 2009; Xypolias, 2009; Xypolias, 2010). If results from the quartz *c*-axis fabric method are indeed representative of much of the ductile flow history for a given rock volume, then this discrepancy may be due to: (1) the behavior of higher aspect ratio grains in high W_k flows at high strain; (2) a lack of grains above R_{crit}, or possibly a combination of both. The discrepancy may be amplified if other contributing factors such as a non-Newtonian rheology (ten Grotenhuis et al., 2002) or imperfect clast–matrix coupling is also a factor (Johnson et al., 2009).

In light of the model presented here it appears that Ghosh and Ramberg's (1976) equations that govern clast rotational behavior in a viscous medium – upon which the rigid grain technique is founded – predict that the method is not equally effective for all flows, particularly at high finite strain. In fact, it appears that most general shear flows continued long enough to develop moderate–high finite strain will tend to produce a clast orientation distribution that will yield a visual estimate of the critical aspect ratio that suggests approximately equal contributions of pure and simple shear components.

Acknowledgments

This paper presents part of the primary author's Ph.D. research. Thorough reviews by Paris Xypolias and an anonymous reviewer helped strengthen and focus the manuscript. Careful editorial handling of Cees Passchier is also appreciated. Funding for this research was provided by National Science Foundation grant EAR 0711207 to RDL.

Appendix A. Supplementary information

Supplementary information associated with this article can be found in the online version at doi:10.1016/j.jsg.2011.05.002.

References

Bailey, C.M., Eyster, E.L., 2003. General shear deformation in the Pinelano Mountains metamorphic core complex, Arizona. Journal of Structural Geology 25, 1883–1893.

Bailey, C.M., Polvi, L.E., Forte, A.M., 2007. Pure shear dominated high-strain zones in basement terranes. In: Hatcher Jr., R.D., Carlson, M.P., McBride, J.H., Martinez Catalan, J.R. (Eds.), 4-D Framework of Continental Crust. Geological Society of America Memoir, vol. 200, pp. 93–108.

Bobyarchick, A.R., 1986. The eigenvalues of steady flow in Mohr space. Tectonophysics 122, 35–51.

Carosi, R., Montomoli, C., Rubatto, D., Visona, D., 2006. Normal-sense shear zones in the core of the Higher Himalayan crystallines (Bhutan Himalaya): evidence for extrusion? In: Law, R.D., Searle, M.P., Godin, L. (Eds.), Channel Flow, Ductile Extrusion and Exhumation in Continental Collision Zones. Geological Society of London, Special Publications, vol. 268, pp. 425–444.

Ghosh, S.K., 1987. Measure of non-coaxiality. Journal of Structural Geology 9, 111–114.

Ghosh, S.K., Ramberg, H., 1976. Reorientation of inclusions by combination of pure and simple shear. Tectonophysics 34, 1–70.

Grasemann, B., Stüwe, K., 2001. The development of flanking structures during simple shear and their use as kinematic indicators. Journal of Structural Geology 23, 715–724.

ten Grotenhuis, S.M., Passchier, C.W., Bons, P.D., 2002. The influence of strain localisation on the rotation behaviour of rigid objects in experimental shear zones. Journal of Structural Geology 24, 485–499.

Holcombe, R.J., Little, T.A., 2001. A sensitive vorticity gauge using rotated porphyroblasts, and its application to rocks adjacent to the Alpine Fault, New Zealand. Journal of Structural Geology 23, 979–989.

Hutton, D.H.W., 1970. A tectonic model for the emplacement of the main Donegal granite, NW Ireland. Journal of the Geological Society of London 139, 615–631.

Jessup, M.J., Law, R.D., Searle, M.P., Hubbard, M.S., 2006. Structural evolution and vorticity of flow during extrusion and exhumation of the Greater Himalayan Slab, Mount Everest Massif, Tibet/Nepal: implications for orogen-scale flow partitioning. In: Law, R., Butler, R., Holdsworth, R., Krabbendam, M., Strachan, R. (Eds.), Channel Flow, Ductile Extrusion and Exhumation in Continental Collision Zones. Geological Society of London, Special Publications, vol. 268, pp. 379–419.

Jessup, M.J., Law, R.D., Searle, M.P., Hubbard, M.S., 2007. The rigid grain net (RGN): an alternative method for estimating mean kinematic vorticity number (W_m). Journal of Structural Geology 29, 411–421.

Johnson, S.E., Lenferink, H.J., Price, N.A., Marsh, J.H., Koons, P.O., West Jr., D.P., 2009. Clast-based kinematic vorticity gauges: the effects of slip at matrix/clast interfaces. Journal of Structural Geology 31, 1322–1339.

Kanagawa, K., 1996. Simulated pressure fringes, vorticity, and progressive deformation. In: De Paor, D.G. (Ed.), Structural Geology and Personal Computers. Computer Methods in the Geosciences, vol. 15. Pergamon, pp. 259–283.

Law, R.D., 2010. Moine Thrust zone mylonites at the Stack of Glencoul: II – results of vorticity analyses and their tectonic significance. In: Law, R., Butler, R., Holdsworth, R., Krabbendam, M., Strachan, R. (Eds.), Continental Tectonics and Mountain Building: the Legacy of Peach and Horne. Geological Society of London, Special Publications, vol. 335, pp. 579–602.

Law, R.D., Searle, M.S., Simpson, R.L., 2004. Strain, deformation temperatures and vorticity of flow at the top of the Greater Himalayan Slab, Everest Massif, Tibet. Journal of the Geological Society of London 161, 305–320.

Malvern, L.E., 1969. Introduction to the Mechanics of a Continuous Medium. Prentice Hall.

Marques, F.O., Coelho, S., 2003. 2-d shape preferred orientations of rigid particles in transtensional viscous flow. Journal of Structural Geology 25, 841–854.

Marques, F.O., Schmid, D.W., Andersen, T.B., 2007. Applications of inclusion behavior models to a major shear zone system: the Nordfjord-Sogn Detachment Zone in Western Norway. Journal of Structural Geology 29, 1622–1631.

Masuda, T., Michibayashi, K., Ohta, H., 1995. Shape preferred orientation of rigid particles in a viscous matrix: reevaluation to determine kinematic parameters of ductile deformation. Journal of Structural Geology 17, 115–129.

McKenzie, D., 1979. Finite deformation during fluid flow. Geophysical Journal of the Royal Astronomical Society 58, 115–129.

Means, W.D., Hobbs, B.E., Lister, G.S., Williams, P.F., 1980. Vorticity and non-coaxiality of progressive deformations. Journal of Structural Geology 2, 371–378.

Mulchrone, K.F., 2007. Shape fabrics in populations of rigid objects in 2D: estimating finite strain and vorticity. Journal of Structural Geology 29, 1558–1570.

Passchier, C.W., 1986. Flow in natural shear zones. Earth and Planetary Science Letters 77, 70–80.

Passchier, C.W., 1987. Stable positions of rigid objects in non-coaxial flow – a study in vorticity analysis. Journal of Structural Geology 9, 679–690.

Passchier, C.W., 1988. Analysis of deformation paths in shear zones. Geologische Rundschau 77, 308–318.

Provost, A., Buisson, C., Merle, O., 2004. From progressive to finite deformation and back. Journal of Geophysical Research 109. doi:10.1029/2001JB001734.

Ramberg, H., 1975. Particle paths, displacement and progressive strain applicable to rocks. Tectonophysics 28, 1–37.

Simpson, C., De Paor, D.G., 1993. Strain and kinematic analysis in general shear zones. Journal of Structural Geology 15, 1–20.

Simpson, C., De Paor, D.G., 1997. Practical analysis of general shear zones using the porphyroclast hyperbolic distribution method: an example from the Scandinavian Caledonides. In: Sengupta, S. (Ed.), Evolution of Geological Structures in Micro- to Macro-scales. Chapman and Hall, pp. 169–184.

Sullivan, W.A., 2008. Significance of transport-parallel strain variations in part of the Raft River shear zone, Raft River Mountains, Utah, USA. Journal of Structural Geology 30, 138–158.

Talbot, C.J., 1970. The minimum strain ellipsoid using deformed quartz veins. Tectonophysics 9, 47–74.

Thigpen, J.R., Law, R.D., Brown, S.J., Lloyd, G.L., Cook, B., 2010. Deformation temperatures, vorticity of flow and strain symmetry in the Loch Eriboll mylonites, NW Scotland: implications for the kinematic and structural evolution of the northernmost moine thrust zone. In: Law, R., Butler, R., Holdsworth, R., Krabbendam, M., Strachan, R. (Eds.), Continental Tectonics and Mountain Building: The Legacy of Peach and Horne. Geological Society of London, Special Publications, vol. 335, pp. 623–662.

Tikoff, B., Fossen, H., 1993. Simultaneous pure and simple shear: the unifying deformation matrix. Tectonophysics 217, 267–283.

Tikoff, B., Fossen, H., 1995. The limitations of three-dimensional kinematic vorticity analysis. Journal of Structural Geology 17, 1791–1794.

Tikoff, B., Fossen, H., 1999. Three dimensional reference deformations and strain facies. Journal of Structural Geology 21, 1497–1512.

Vissers, R.J.M., 1989. Asymmetric quartz *c* -axis fabrics and flow vorticity: a study using rotated garnets. Journal of Structural Geology 11, 231–244.

Wallis, S.R., 1992. Vorticity analysis in a metachert from the Sanbagawa Belt, SW Japan. Journal of Structural Geology 14, 271–280.

Wallis, S.R., 1995. Vorticity analysis and recognition of ductile extension in the Sanbagawa Belt, SW Japan. Journal of Structural Geology 17, 1077–1093.

Wallis, S.R., Platt, J.P., Knott, S.D., 1993. Recognition of syn-convergence extension in accretionary wedges with examples from the Calabrian arc and the eastern Alps. American Journal of Science 293, 463–495.

Xypolias, P., 2009. Some new aspects of kinematic vorticity analysis in naturally deformed quartzites. Journal of Structural Geology 31, 3–10.

Xypolias, P., 2010. Vorticity analysis in shear zones: a review of methods and applications. Journal of Structural Geology 32, 2072–2092.

Xypolias, P., Doutsos, T., 2000. Kinematics of rock flow in a crustal-scale shear zone: implications for the orogenic evolution of the southwestern Hellenides. Geological Magazine 137, 81–96.

Xypolias, P., Kokkalas, S., 2006. Heterogeneous ductile deformation along a mid-crustal extruding shear zone: an example from the external Hellenides (Greece). In: Law, R.D., Searle, M.P., Godin, L. (Eds.), Channel Flow, Ductile Extrusion and Exhumation in Continental Collision Zones. Geological Society of London, Special Publications, vol. 268, pp. 497–516.

Xypolias, P., Koukouvelas, I.K., 2001. Kinematic vorticity and strain patterns associated with ductile extrusion in the Chelmos shear zone (External Hellinides, Greece). Tectonophysics 338, 59–77.